RSC Advances

PAPER

View Article Online
View Journal | View Issue

Cite this: *RSC Adv.*, 2026, **16**, 19255

Interfacial ion aggregation at SiO_2 nanoparticles enhances thermal energy storage of chloride molten salts: a molecular dynamics study

Chao Wang,†[a] Haowei Hu,†[a] Qin Li,*[ab] Lin Guo *[c] and Mingyang Yang*[d]

Chloride molten salts have emerged as a promising heat transfer medium for concentrated solar power plants owing to their low cost. However, their widespread adoption has been hindered by limited specific heat capacity and thermal conductivity. In this work, the thermal properties of binary chloride molten salts (NaCl–KCl) were enhanced by adding varying amounts of amorphous SiO_2 nanoparticles. Molecular dynamics simulations were employed to investigate the effects of many-particle effects of SiO_2 nanoparticles on the thermal properties of molten salts instead of the normal one-particle doped model. The underlying mechanism for the improved thermal performance is elucidated by examining the evolution of microstructure, thermal diffusivity, and energy variations. Results demonstrate that with increasing nanoparticle content, the viscosity, specific heat capacity, and thermal conductivity are enhanced by approximately 51.21%, 8.25%, and 7.08%, respectively. It is revealed that the selective adsorption of Na^+ and K^+ ions onto the surface of SiO_2 nanoparticles leads to the formation of a compressed interfacial layer roughly 6 Å in thickness, which contributes to the enhancement in thermal conductivity. This study offers valuable insights for the design and optimization of chloride molten salt-based nanocomposites for next-generation CSP systems.

Received 30th December 2025
Accepted 31st March 2026

DOI: 10.1039/d5ra10091g

rsc.li/rsc-advances

1 Introduction

In the rapid urbanization and modernization process of the past few decades, people have become increasingly concerned about environmental pollution caused by the use of fossil energy. This concern has further driven the urgent need for sustainable energy alternatives.[1] Solar energy has attracted much attention due to its huge potential reserves.[2,3] Large-scale photovoltaic cell arrays directly convert solar energy into electricity, which has significant advantages such as being renewable and clean without pollution. This provides an important way to alleviate the energy crisis and reduce greenhouse gas emissions.[4] According to the International Energy Agency (IEA) report, the installed capacity of solar power generation increased from 586 GW in 2019 to 1467 GW in 2023, with a compound annual growth rate of 25.8%, and is expected to reach 5365 GW by 2029.[5] However, as an intermittent energy source, the power generation of solar energy is greatly affected by factors such as day and night alternation and weather changes, showing obvious discontinuity and instability. Thermal energy storage systems (TES) are technologies used to temporarily store thermal energy, which can release thermal energy when needed, thus realizing the temporal mismatch between energy supply and demand. Concentrated solar power (CSP) technology generates thermal energy for power generation by concentrating solar radiation. With the help of its integrated TES system, it has realized dispatchable solar power generation and shown broad application prospects.[6,7] To achieve stable supply of solar energy, energy storage technology has become a key support for the development of concentrated solar power stations.[8]

Among many energy storage technologies, molten salt energy storage stands out with its unique properties. Molten salts have high melting points, good thermal stability, large heat capacity, and moderate viscosity, which enable efficient heat storage and release at high temperatures. They are highly compatible with the high-temperature heat collection systems of CSP plants and have become one of the most promising energy storage media in large-scale solar thermal power generation systems.[9,10] Currently, nitrate and carbonate salts are more commonly used as energy storage materials. Nitrate salts have advantages such as low melting points and large specific heat capacities, but their heat transfer coefficients are low, and their working temperature range is narrow (300–600 °C), making it difficult to adapt to higher temperature conditions.[11–13] Carbonate salts have relatively high thermal conductivity and low corrosiveness, but they are prone to

[a]*Engineering Research Center of Building Energy Efficiency Control and Evaluation, Ministry of Education, Anhui Jianzhu University, Hefei 230022, China*

[b]*School of Materials and Chemical Engineering, Anhui Jianzhu University, Hefei 230601, China. E-mail: liqin053@163.com*

[c]*School of Energy and Power Engineering, Shandong University, Jinan 250061, China*

[d]*School of Resources Engineering, Xi'an University of Architecture and Technology, Xi'an, 710055, China*

† These authors contributed equally.

decomposition when heated, and their viscosity is very high.[14,15] At the same time, the working temperature requirements for CSP plants are increasing. The U.S. Department of Energy has launched a third-generation high-temperature CSP project, with the operating temperature of the thermal power generation system reaching above 700 °C. Nitrate and carbonate salts are not suitable for higher working temperatures, so there is an urgent need for high-performance heat transfer and energy storage media in the high-temperature range.[16] Compared with the above two types of molten salts, chloride molten salts that have developed in recent years have advantages such as a wide adjustable melting point range (about 500–800 °C) and higher thermal stability (they can remain stable at around 800 °C).[17,18] Although the corrosion of equipment by chloride molten salts at high temperatures will be enhanced, scholars have proposed effective strategies such as molten salt purification treatment and the use of corrosion inhibitors to control the corrosion rate of equipment by molten salts, effectively promoting the practical application of chloride molten salts.[19–21] Chloride salts are widely considered to be the most promising high-temperature energy storage materials for next-generation CSP plants.[22]

Most inorganic salts have the advantages of large phase change enthalpy and high density, but they still have problems such as low thermal conductivity and small specific heat capacity.[23] These problems can affect the heat exchange rate, reduce the heat storage capacity, and greatly limit the application of latent heat energy storage technology in CSP plants. In order to overcome these problems, domestic and foreign experts and scholars have conducted research on the preparation of molten salts and the strengthening of their thermophysical properties, and found that adding high thermal conductivity materials to molten salt materials is an effective way to improve the heat transfer and heat storage properties of molten salts, such as expanded graphite, nanoparticles, *etc.*[24–26]

To study the influence of nanoparticles on the thermal properties of molten salts, a series of experiments have been carried out by relevant researchers. Tao *et al.*[27] added four different microstructured carbon nanomaterials to binary carbonate eutectic salts and found that single-walled carbon nanotubes can increase thermal conductivity by 56.98%, making it the best additive. Cui *et al.*[28] investigated the effects of carbon nanofibers (CNF) and carbon nanotubes (CNT) on the thermal properties of phase change energy storage materials. The results showed that 10 wt% of CNF and CNT can increase the thermal conductivity of composite phase change materials by more than 20%, and CNF is more effective due to its better dispersibility. Qiao *et al.*[29] found that SiO_2 nanoparticles can increase the specific heat capacity C_p of nitrates between 623 K and 641 K, with the highest increase of 27.6% in the specific heat of $NaNO_3$. J. Navas *et al.*[30] added copper and nickel nanoparticles to nanofluids, and the thermal conductivity of copper nanofluids was 11% higher than that of the base fluid. Aljaerani *et al.*[31] doped KNO_3, $NaNO_2$, and $NaNO_3$ ternary nitrate molten salts with CuO nanoparticles of different mass fractions and concluded that the optimal concentration was 0.1 wt%, with a specific heat capacity increase of 5.6%. Han *et al.*[32] mixed Al_2O_3, ZnO, and CuO nanoparticles with $MgCl_2$–KCl–NaCl ternary chloride salts, and Al_2O_3 nanoparticles can increase the thermal conductivity λ by 48%. Rizvi *et al.*[33] added SiO_2 nanoparticles to the $LiCO_3$–K_2CO_3 binary salt, and the specific heat capacity was 25.1% higher than that of pure molten salt. The enhancement of C_p is mainly attributed to the dendritic structure around high zeta potential cation nanoparticles. Despite a large number of studies, it is still challenging to elucidate the mechanism of thermal performance enhancement due to the difficulty of analyzing ion movement through experiments.

Therefore, molecular dynamics (MD) simulations have also been applied to reveal the mechanism of thermal performance enhancement from a microscopic perspective. Song *et al.*[34] added SiO_2 nanoparticles to the binary molten carbonate Na_2CO_3/K_2CO_3. The results showed that the addition of SiO_2 nanoparticles can significantly increase the specific heat capacity of the alkaline salts by up to 24.38%. The improvement in thermal performance is attributed to the dense interfacial layer formed by ions on the outer surface of the nanoparticles, and is also related to the changes in the system's microstructure after the addition of nanoparticles. Qiao *et al.*[35] found through MD simulations that SiO_2 nanoparticles can form a compressed layer in nitrates, leading to an increase in the density and specific heat capacity of nitrates. J. Seo *et al.*[36] added SiO_2 nanoparticles and acicular Li_2CO_3 nanomaterials to K_2CO_3–Li_2CO_3 eutectic salts. The results show that both significantly increased the specific heat of the eutectic salts, and it is speculated that this is due to the formation of a dense layer around SiO_2. Zhou *et al.*[37] found that the thermal conductivity of NaCl with Al_2O_3 nanoparticles increased due to the enhanced collisions within the dense ion layer around the nanoparticles. Yang *et al.*[38] found that the specific heat capacity of chloride molten salts containing SiO_2 nanoparticles first increased and then decreased with the doping ratio of SiO_2, reaching a maximum at 1 wt% SiO_2. The increase in the specific heat capacity of molten salt-based nanofluids may be due to the mismatch in the relative number density of cations and anions in the SiO_2 interfacial layer. Liu *et al.*[39] found that the addition of SiO_2 nanoparticles enhanced the specific heat capacity of solar salt, probably because the accumulation of K^+ ions near SiO_2 particles formed a compressed interfacial layer. Despite extensive MD studies on the thermal performance enhancement of nanoparticles, there is still a lack of comprehensive exploration of the mechanism of thermal performance enhancement under high-temperature conditions from the perspective of microscopic structure and energy changes as well as thermal diffusion properties.

Due to the difficulty in experimentally investigating the microscopic motion of ions, current molecular dynamics (MD) simulations lack research on the impact of adding multiple nanoparticles on the thermal properties of molten salts, as well as comprehensive studies on the principles of thermal property enhancement. This paper is based on a binary chloride molten salt (NaCl–KCl) composed in a molar ratio of 1 : 1, with the addition of multiple amorphous SiO_2 nanoparticles. The study investigates the effects of different numbers of amorphous SiO_2 nanoparticles (1, 3, 5, and 8) on the thermal conductivity, viscosity, and specific heat capacity of the NaCl–KCl composite thermal energy storage material under high-temperature conditions (1000 K to 1800 K, with intervals of

100 K) using molecular dynamics (MD) simulation methods. It also explores the principles of how the addition of multiple nanoparticles affects the microstructure of the molten salt and enhances its thermal properties, from the perspectives of microscopic structural changes, thermal diffusion properties, and energy variations.

2 Method

2.1. Model and methodology

The initial binary chloride molten salt of NaCl–KCl was composed of NaCl and KCl in a molar ratio of 1 : 1, containing 4222 Na^+, 4222 K^+, and 8444 Cl^- ions. The simulation box dimensions (L_x, L_y, L_z) were all set to 90 Å to eliminate the influence of finite size on the prediction of thermal properties. Subsequently, using the LAMMPS software and the molecular templates for Na, K, and Cl, these three types of ions were randomly distributed within the cubic box to form the binary chloride molten salt.

Referring to relevant literature, a crystalline SiO_2 model was constructed using the MS software. Through heating and cooling operations, an amorphous SiO_2 model was ultimately obtained.[40,41] A SiO_2 nanoparticle model with a radius of 10 Å was then cut out from the amorphous SiO_2 model. Subsequently, the SiO_2 nanoparticle model exported from Materials Studio (MS) was converted into a simulation system data file readable by LAMMPS. Amorphous SiO_2 nanoparticles were randomly doped into the simulation box in quantities of 1, 3, 5, and 8 to generate the SiO_2/(NaCl–KCl) molten salt nanofluid model, as shown in Fig. 1.

2.2. Force field

In this study, the Fumi–Tosi potential is employed to describe the interactions between Na^+, K^+, and Cl^- ions.[42] It can be expressed by eqn (1):

$$U_{ij} = \frac{q_i q_j}{r_{ij}} + A_{ij}\exp\left(\frac{\sigma_{ij} - r_{ij}}{\rho}\right) - \frac{C_{ij}}{r_{ij}^6} - \frac{D_{ij}}{r_{ij}^8} \quad (1)$$

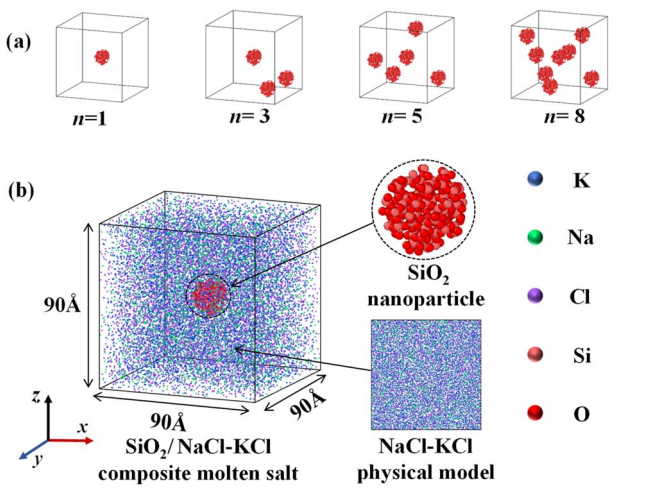

Fig. 1 (a) Randomly distributed SiO_2 nanoparticles with varied numbers (n = 1–8) (b) simulation settings of NaCl–KCl molten salt/SiO_2 nanoparticle composite system.

Table 1 Fumi–Tosi potential parameters of binary NaCl–KCl[43]

	K–K	K–Na	Na–Na	K–Cl	Na–Cl	Cl–Cl
A_{ij} (Kcal mol^{-1})	6.08	6.08	6.08	4.86	4.86	3.65
σ_{ij} (Å)	2.926	2.663	2.340	3.048	2.755	3.170
C_{ij} (Kcal mol^{-1} Å^6)	349.46	91.88	24.16	690.30	161.07	1729.35
D_{ij} (Kcal mol^{-1} Å^8)	345.15	63.02	11.51	1049.83	199.90	3473.08

where q_i q_j are the charges of the ions, r_{ij} is the distance between them. The exponential repulsive term $A_{ij}\exp\left(\frac{\sigma_{ij} - r_{ij}}{\rho}\right)$ is used to describe the short-range repulsion between ions. The parameter A_{ij} is used to adjust the strength and range of the repulsion, and σ_{ij} is the sum of the ionic radii. The term $\frac{C_{ij}}{r_{ij}^6} - \frac{D_{ij}}{r_{ij}^8}$ is used to describe the long-range attraction between ions, where the $\frac{C_{ij}}{r_{ij}^6}$ term represents dipole–dipole interactions, and the $\frac{D_{ij}}{r_{ij}^8}$ term represents dipole–quadrupole interactions (Tables 1–3).

The energy of the amorphous SiO_2 nanoparticle system consists of bonding energy and non-bonding energy. Among them, the non-bonding energy is calculated using the BKS potential energy. Currently, this method is widely used to describe the interactions between atoms in SiO_2 nanoparticles.[41,44] The expression of the BKS potential can be represented as eqn (2):

$$E_{\text{non-bonded}} = A_{ij}e^{-\frac{r_{ij}}{\rho_{ij}}} - \frac{C_{ij}}{r_{ij}^6} + \frac{q_i q_j}{r_{ij}} \quad (2)$$

Among them, A_{ij} and C_{ij} are used to adjust the strength and range of the interaction between different atoms. r_{ij} is the distance between atom i and atom j, q_i and q_j are the charges of the atoms.

The bonding energy can be calculated by the following formula, where K_b and K_θ are the force constants of the bond length term and the bond angle term, respectively, and R and θ are the bond length and bond angle constants, respectively.

Table 2 Non-bonded parameters[35] and bonded[45] parameters of SiO_2

Non-bonded parameters			
	A_{ij} (Kcal mol^{-1})	ρ_{ij} (Å)	C_{ij} (Kcal mol^{-1} Å^6)
Si–Si	72 460.64	0.351	14 415.29
O–O	15 170.70	0.386	617.24
Si–O	33 155.37	0.368	2982.90

Bonded parameters		
Si–O	K_b (Kcal mol^{-1} A^{-2}) = 285.0	R_0 (Å) = 1.68
O–Si–O	K_θ (Kcal mol^{-1} rad^{-2}) = 100.0	θ_0 (°) = 109.5
Si–O–Si	K_θ (Kcal mol^{-1} rad^{-2}) = 100.0	θ_0 (°) = 149.0

Table 3 L-J potential parameters for the chloride salt and silica in the present study[45,46]

Atom	ε_{ij} (Kcal mol^{-1})	σ_{ij} (Å)
Na	0.0860	2.730
K	0.0800	2.760
Cl	0.1001	4.400
Si	0.0400	4.053
O	0.2280	2.860

$$E_{\text{bond}} = K_b(R - R_0)^2 + K_\theta(\theta - \theta_0)^2 \quad (3)$$

The interaction between chloride salts and SiO_2 is described using the Coulomb term of the Lennard-Jones (LJ) potential.

$$u = 4\varepsilon_{ij}\left[\left(\frac{\sigma_{ij}}{r_{ij}}\right)^{12} - \left(\frac{\sigma_{ij}}{r_{ij}}\right)^{6}\right] + \frac{q_i q_j}{r_{ij}} \quad (4)$$

q_i and q_j represent the charges of the particles, while r_{ij} denotes the distance between them. ε_{ij} represents the depth of the potential energy, indicating the strength of the interaction between the particles. σ_{ij} is the diameter of the particles, representing the distance scale between them. The term $\left(\frac{\sigma_{ij}}{r_{ij}}\right)^{12}$ represents the repulsive force between the particles, and the term $\left(\frac{\sigma_{ij}}{r_{ij}}\right)^{6}$ represents the attractive force between them. In the system, the charge values of Na, K, Cl, Si, and O atoms are +1, +1, −1, +1.91, and −0.95 respectively. The interaction between chloride salts is truncated at a distance of 15 Å, while the interaction within non-crystalline SiO_2 and the interaction between chloride salts and SiO_2 are truncated at a distance of 10 Å.

2.3. Simulation details

All simulation tasks were conducted on the open-source molecular dynamics simulation platform LAMMPS. The constructed model includes molten chloride salts and amorphous SiO_2 nanoparticles. Periodic boundary conditions (PBC) were applied in the *x*, *y*, and *z* directions to maintain a stable number of particles within the system and effectively avoid boundary effects. The initial velocities of the particles were randomly distributed and followed a Gaussian distribution. The velocity-Verlet algorithm was used to solve Newton's equations of motion to obtain the atomic trajectories. For long-range interactions, the Ewald method for long-range dispersion was employed. The time step in the simulation was set to 0.002 ps. Temperature control was implemented using the Nosé–Hoover thermostat, while pressure control was achieved *via* the Parrinello–Rahman barostat. To make the simulation system more realistic, an annealing process was performed at the beginning of the simulation: the system was heated from 300 K to 1800 K, held at equilibrium at 1800 K for 1 ns, and then gradually cooled to the target temperature. All the above simulation processes were carried out under *NPT* ensemble conditions at a pressure of 0.1 MPa with a temperature change rate of 10 K ps^{-1}. Subsequently, at each set target

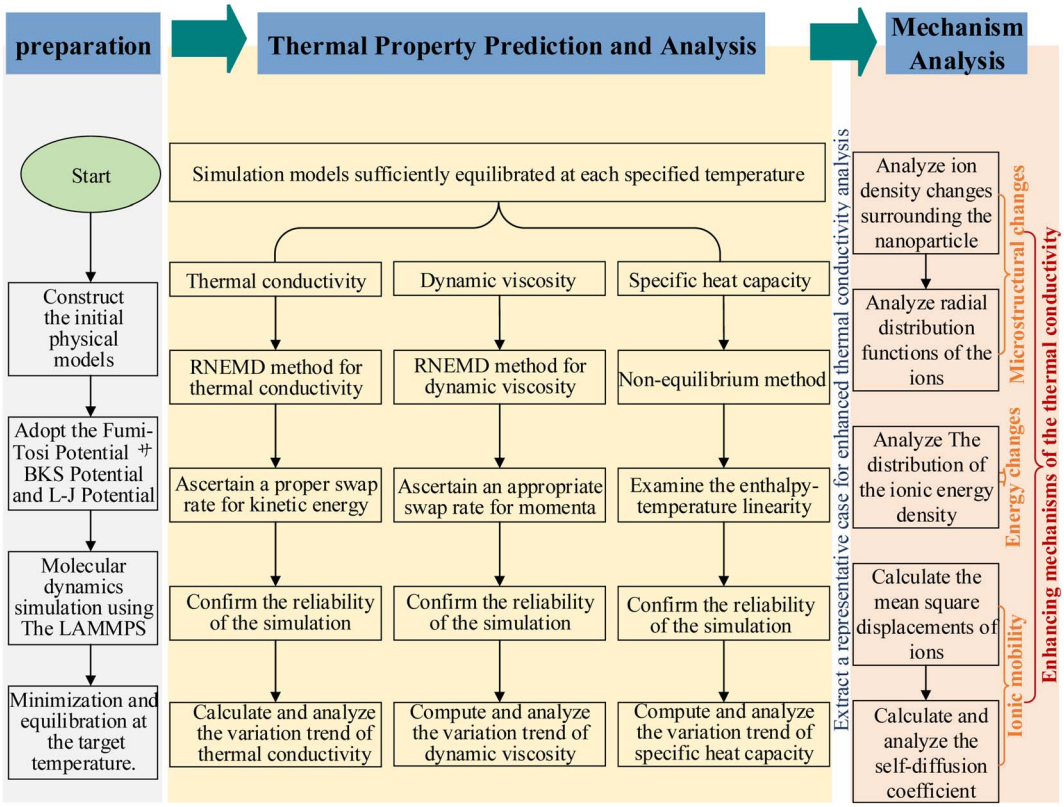

Fig. 2 Simulation methodology in this work.

temperature point, the system was run for 1 ns under *NVT* ensemble conditions to ensure the system reached equilibrium. Finally, thermal performance indicators and various energy data were calculated and analyzed, and the results were compared with corresponding experimental values to ensure the reliability and accuracy of the obtained data. The technical route of this work is shown in Fig. 2.

3 Results and discussion

3.1. Thermal conductivity

The thermal conductivity of molten salt materials is crucial for their heat storage characteristics because high thermal conductivity enables rapid heat absorption during storage and quick and uniform heat release during discharge. Therefore, it is essential to study the thermal conductivity of CTES material. Due to the challenges of measuring thermal conductivity experimentally at ultra-high temperatures, MD simulations have been proven to be a reliable method for predicting material thermal conductivity. For the thermal conductivity calculations, the system was first equilibrated in the *NVT* ensemble for 1 ns, followed by production runs in the *NVE* ensemble. In this study, the Müller-Plathe (velocity exchange) method was used to predict thermal conductivity, as illustrated in Fig. 3.[47] The entire system was divided into 20 layers along the Z direction, with the central region defined as the hot zone and the regions on both sides of the system defined as the cold zones. The velocities of atoms moving slowly in the hot zone were exchanged with those of atoms moving quickly in the cold zones, resulting in energy transfer. After several steps, when the energy exchange rate equaled the conduction rate and the temperature distribution across the system reached equilibrium, the temperature gradient was statistically analyzed to obtain the thermal conductivity data. By calculating the thermal conductivity at different temperatures for varying numbers of SiO_2 nanoparticles, the effects of the number of SiO_2 nanoparticles and temperature changes on thermal conductivity were determined. The thermal conductivity λ can be calculated using eqn (5).

$$\lambda = -\frac{\sum_{\text{transfer}} \frac{1}{2} m\left(v_h^2 - v_c^2\right)}{2\Delta t L_x L_y (\partial T/\partial Z)} \quad (5)$$

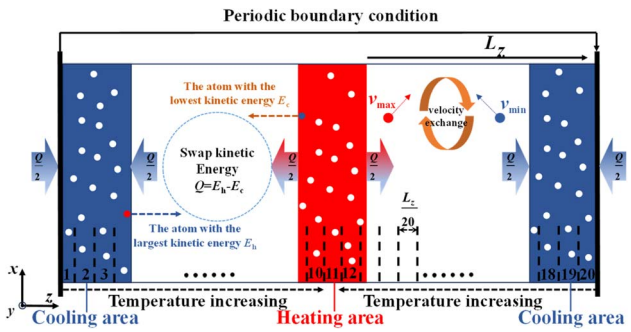

Fig. 3 Schematic diagram of the RNEMD method for simulating λ by forming a temperature gradient through velocity exchange.

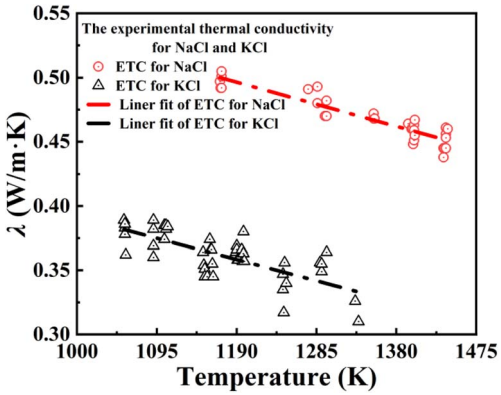

Fig. 4 The experimental thermal conductivity for NaCl and KCl in ref. 48 and the resulting linear fit.

Among them, v_h and v_c represent the velocities of the atoms in the hot zone and the cold zone respectively. m is the mass of the particle, Δt is the time for energy transfer. L_x and L_y are the lengths of the system in the x and y directions respectively. $\partial T/\partial Z$ indicates the temperature change per unit distance in the Z direction. The temperature gradient is calculated based on the temperature difference between the hot zone and the cold zone. By comparing the results of the thermal conductivity calculated by the MD method with the experimental data, the accuracy of the Reverse Non-Equilibrium Molecular Dynamics (RNEMD) method for calculating the thermal conductivity λ of the chloride salt melt is verified.[48] As shown in Fig. 4. At the same time, the thermal conductivities of KCl and NaCl measured in the experiment at different temperatures were statistically analyzed, and a linear fit was performed between temperature and thermal conductivity, and the results are shown in Table 4.

$$\lambda = A \times T + B \quad (6)$$

Finally, the thermal conductivity of the KCl–NaCl composite molten salt was calculated using eqn (7).[49]

$$\lambda_{KNaCl_2} = w_{KCl}\lambda_{KCl} + w_{NaCl}\lambda_{NaCl} - (\lambda_{NaCl} - \lambda_{KCl})[1 - (w_{NaCl})^{1/2}] \quad (7)$$

Here, λ_{KCl} and λ_{NaCl} represent the thermal conductivity coefficients of KCl and NaCl respectively. w_{KCl} and w_{NaCl} represent the mass fractions of KCl and NaCl respectively. The calculated thermal conductivity results are shown in Fig. 5(a). The simulated values of the thermal conductivity of the molten salt in the range of 1000–1400 K are in good agreement with the experimental values, with the maximum relative error being 9.66% occurring at 1200 K. By comparing the experimental and

Table 4 Parameters in the eqn (7) of NaCl and KCl thermal conductivity

Molten salt	$A \times 10^{-4}$	B
KCl	1.7429 ± 0.2489	0.5657
NaCl	1.8176 ± 0.1390	0.7127

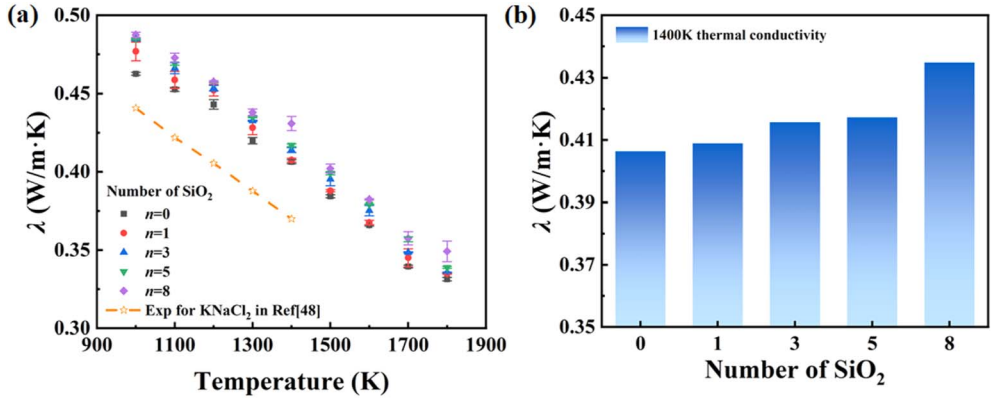

Fig. 5 (a) The thermal conductivity results calculated by MD simulation and experiment of CTES systems at different temperatures. (b) The thermal conductivity results calculated by MD simulation of CTES systems at 1400 K.

simulated results in Fig. 4 and 5(a), it is demonstrated that the selected simulation method and force field type can be used to study the thermal conductivity issues addressed in this paper.

Specifically, the simulations revealed that the thermal conductivity increased with the addition of SiO_2 nanoparticles at different temperatures. At 1000 K, increasing the number of SiO_2 nanoparticles did not significantly enhance the thermal conductivity. At 1400 K, as the number of added SiO_2 nanoparticles increased from 1 to 8, the thermal conductivity changes are shown in Fig. 5(b), with increases of 0.62% and 7.08%, respectively. It is noteworthy that the enhancement of thermal conductivity by adding eight particles is 11.52 times that of adding one particle. Adding eight particles can effectively improve the heat transfer efficiency of the molten salt, reduce the internal temperature gradient of the molten salt, and make the temperature distribution within the molten salt more uniform.

The calculation of thermal conductivity does indeed involve statistical errors, especially at high temperatures (1700 K) or low temperatures (1000 K) where system fluctuations are significant—this is an inherent limitation of molecular dynamics simulations. The 'inversion' phenomenon observed between adding 8 particles *versus* 1 particle at certain temperatures likely stems from a complex mechanism involving the dominance of many-body effects superimposed with statistical errors.

3.2. Dynamic viscosity

The calculation of molten salt viscosity can be used to determine its fluidity, predict flow resistance, affect heat transfer efficiency, and assist in optimizing the structural design of heat exchangers and other equipment. Therefore, it is necessary to conduct research on the influence of adding different amounts of particles on the viscosity of molten salt. For the viscosity calculations, the system was equilibrated in the *NVT* ensemble for 1 ns, followed by production runs in the *NVT* ensemble. In this paper, the prediction of viscosity adopts the RNEMD method proposed by Müller-Plathe in 1999.[50] The schematic diagram of the viscosity calculation principle is shown in Fig. 6. The entire system is divided into 20 regions along the *z*-axis. The velocity gradient is constructed by exchanging the *x*-direction momentum components of the atoms in the 1st and 20th regions and the 11th region, thereby forming a shear field. At the same time, the momentum transfer quantity in the *z*-direction is counted for calculation.

Based on the calculation results, the viscosity of the system varies with temperature and the quantity of SiO_2 nanoparticles. The viscosity can be calculated using eqn (8).

$$\eta = -\frac{\sum_{\text{transfer}} (P_{x,1} - P_{x,11})}{2\Delta t L_x L_y (\partial v_x / \partial Z)} \quad (8)$$

Here, $P_{x,1}$ and $P_{x,11}$ represent the *x*-component of the exchanged momentum in regions 1 and 11 respectively. $\partial v_x/\partial Z$ indicates the change in velocity (in the *x*-direction) per unit distance in the *z*-direction.

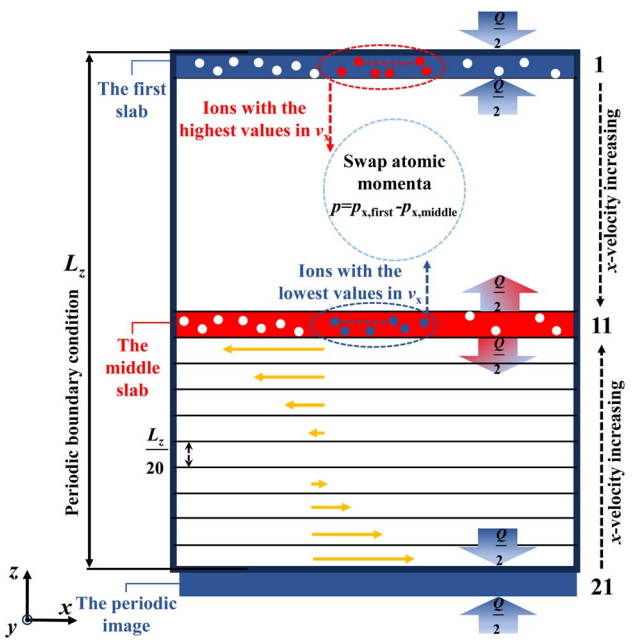

Fig. 6 Schematic diagram of the RNEMD method for simulating η by forming a velocity gradient through velocity exchange.

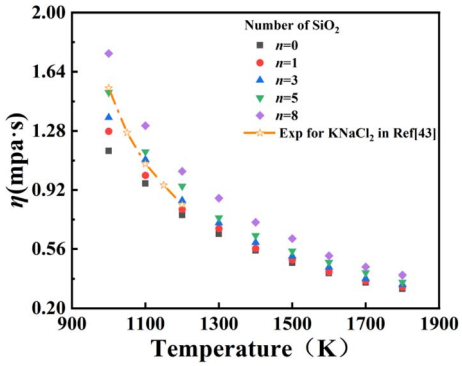

Fig. 7 The viscosity results calculated by MD simulation and experiment of CTES systems at different temperatures.

The viscosity characteristics of CTES material are significantly affected by temperature changes. Fig. 7 shows the trend of viscosity variation with temperature. The viscosity data obtained through the RNEMD method were compared with the experimental data measured using the oscillating ball method.[43] As the temperature gradually increased, the agreement between the simulation data and the experimental data significantly improved. Especially at 1200 K, the error between the two was only 7.6%, which proves that the RNEMD method is reliable for calculating the viscosity of chloride-based fluids.

The viscosity of CTES material decreases with increasing temperature, as the rise in temperature weakens the association between cations and anions, reducing the fluid's resistance to shear deformation. At the same temperature, the addition of SiO_2 nanoparticles increases the viscosity because the nanoparticles enhance the association between cations and anions. Specifically, at 1000 K, the addition of 1, 3, 5, and 8 SiO_2 nanoparticles increases the viscosity by 10.36%, 17.62%, 30.74%, and 51.21%, respectively. At 1800 K, the same doping levels result in viscosity increases of 4.09%, 8.81%, 13.21%, and 26.42%, respectively. This indicates that the effect of SiO_2 nanoparticle doping on viscosity diminishes with increasing temperature. Although increased viscosity can reduce heat transfer efficiency, this effect gradually decreases at high temperatures. This work elucidates the microscopic correlation mechanism between interfacial ionic layer formation and viscosity increase, providing a theoretical foundation for subsequent comprehensive evaluation of nanofluid engineering applicability through performance evaluation criteria.

3.3. Specific heat capacity

The specific heat capacity is used to measure the heat storage capacity of CTES material during the temperature variation process. The calculation is carried out through formula (9) to obtain the result.

$$C_p = \left(\frac{\Delta Q}{\Delta T \times V \times \rho}\right)_p \quad (9)$$

Here, ΔQ represents the total energy absorbed by the system, ΔT is the range of temperature increase, V and ρ are the volume and density of the simulated system. Firstly, the system is equilibrated under the *NPT* ensemble at 1000 K, and then it is heated from 1000 K to 1800 K. The temperature and total energy changes during the heating process are recorded, and a linear fit is performed to obtain $\frac{\Delta Q}{\Delta T}$ to ensure the accuracy of the heat capacity calculation. The result of the linear fit is shown in Fig. 8(a). The total energy gradient is determined, and the subscript numbers indicate the number of added SiO_2 nanoparticles. Finally, the heat capacity is calculated using $\frac{\Delta Q}{\Delta T}$, V and ρ, as shown in Fig. 8(b).

Firstly, the specific heat capacity of the NaCl–KCl composite molten salt obtained from the simulation calculation is compared with the experimental measurement data. The high-temperature (T greater than 1000 K) experimental data of pure chloride molten salts are from ref. 51 and 52, where the specific heat capacity of NaCl is 1.1559 J $(g\ K)^{-1}$ and that of KCl is 0.9872 J $(g\ K)^{-1}$. Then, the specific heat capacity of the mixed molten salt can be derived from the calculation formula (10):

$$C_{p\_KNaCl_2} = x_{NaCl} \times C_{p\_NaCl} + x_{KCl} \times C_{p\_KCl} \quad (10)$$

Here, x_{NaCl} and x_{KCl} represent the mole fractions of NaCl and KCl respectively. The experimental value of the specific heat

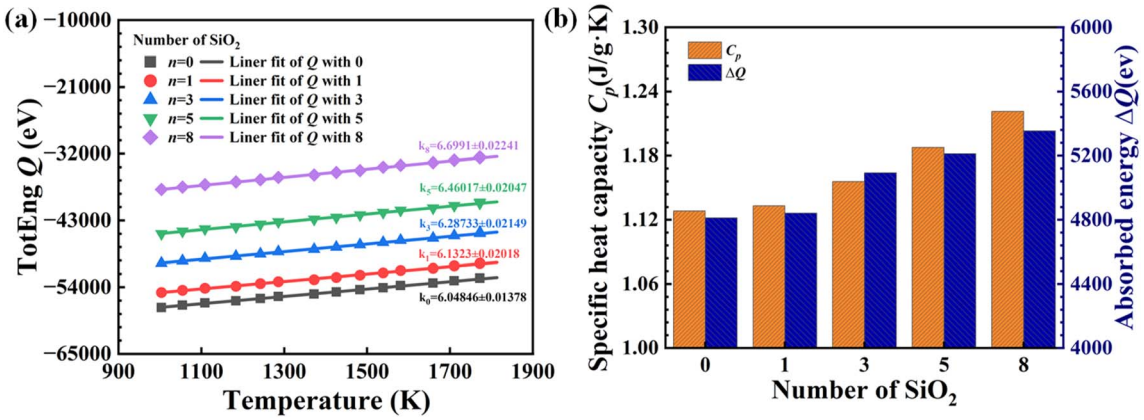

Fig. 8 (a) The total energy of CTES systems counted by MD simulation during the heating process. (b) The absorbed energy ΔQ and specific heat capacity C_p of CTES systems.

capacity of the mixed molten salt is 1.0716 J (g K)$^{-1}$, while the simulation result is 1.1282 J (g K)$^{-1}$. The specific heat capacity of the NaCl–KCl composite molten salt simulated by the method is 5.28% different from the experimental value. This indicates that the selected simulation method and force field type can be used to study the specific heat capacity issues involved in this paper.

Fig. 8(b) shows the calculated results of the absorbed energy and specific heat capacity during the heating process. It is evident that increasing the number of nanoparticles increases the energy absorbed by the molten salt system within the same heating interval, indicating that the use of nanoparticles can effectively enhance the material's heat storage capacity. As the number of SiO_2 nanoparticles increases from 0 to 1, 3, 5, and 8, the specific heat capacity of the molten salt increases by 0.443%, 2.46%, 5.27%, and 8.25%, respectively. Notably, the enhancement of specific heat capacity by adding eight particles is approximately 19 times that of adding one particle. The absorbed energy of the molten salt increases by 0.60%, 5.84%, 8.30%, and 11.25%, respectively.

3.4. Microstructure evolution

In order to investigate the influence of the incorporated nanoparticles on the distribution of ions in the molten salt, the atomic number density n in the outer spherical region of SiO_2 nanoparticles was calculated using the MATLAB program. Since the SiO_2 nanoparticles are in a non-fixed state, the position of their center of mass needs to be determined first. Then, by calculating the distance between the basic liquid ions and the center of mass, and subtracting the radius of the nanoparticle, the distance d between the basic liquid ions and the surface of SiO_2 can be obtained.[53] Within the distance range of 0–10 Å, for the spherical shell region with a thickness of 1 Å, the number N of basic liquid ions in this region was counted. The number density is obtained by dividing the number of ions in the spherical shell region by the volume of the region, that is, $n = N/V$.

Taking a temperature of 1400 K as an example, Fig. 9 shows the function graph of the molten salt density as a function of distance when a single nanoparticle is added. From the graph, it can be seen that when d is small, the density increases with the increase of distance, reaching the average number concentration level of the NaCl–KCl composite molten salt at 3.5 Å. This is because some basic fluid ions are adsorbed on the surface of the nanoparticles. In the distance range of 3.5 Å to 6 Å, the density is significantly higher than the average density of the NaCl–KCl composite molten salt, which indicates that a compressed interface layer with a thickness of approximately 6 Å has been built on the surface of the nanoparticles. Once d exceeds 6 Å, the density of the basic liquid is consistent with the average density of the NaCl–KCl molten salt, thus indicating that the influence of nanoparticles on the local microstructure is limited to the area outside the surface of the nanoparticles by about 6 Å.

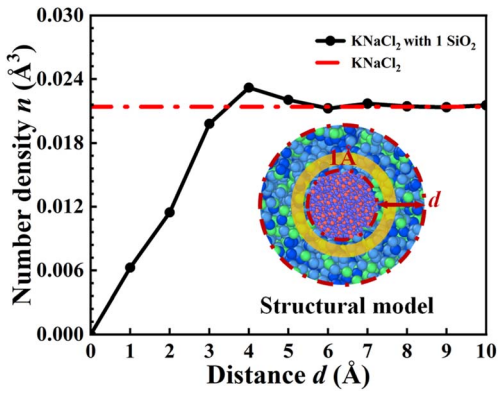

Fig. 9 Distribution of number density with distance d. (insets) SiO_2 spherical shell structure model.

The radial distribution function $g(r)$ is an important parameter for studying the orderliness of the microscopic structure of substances. By analyzing the radial distribution function, the changes in the microscopic structure of the basic nanofluid before and after adding 0 or 8 SiO_2 nanoparticles at 1400 K were investigated, as well as the $g(r)$ of Na–Cl with different amounts of SiO_2 nanoparticles added. The expression of the radial distribution function $g(r)$ is as shown in eqn (11):

$$g_{ij}(r) = \frac{1}{4\pi\rho_j r^2}\left[\frac{\mathrm{d}N_{ij}(r)}{\mathrm{d}r}\right] \quad (11)$$

Here, ρ_j represents the density of atom j, and N_{ij} is the average number of type j atoms in a spherical region with a radius r of type i atom centers.

Fig. 10(a) shows the calculation results of the $g(r)$ of the basic liquid ions before and after adding 8 nanoparticles at a temperature of 1400 K. The RDFs all exhibit the following characteristics: the fluctuation amplitude after the first peak gradually becomes less and less, and it approaches 1 at a greater distance, indicating that the nanofluid presents a clear short-range ordered and long-range disordered amorphous structure in the molten state. After adding nanoparticles, the area of the $g(r)$ curve for all basic fluid ions pairs has increased, which means that the coordination number has increased, thereby confirming the existence of the compressed interface layer shown in Fig. 9. Fig. 10(b) presents the difference in radial distribution functions between the 8-nanoparticle and 0-nanoparticle systems. Positive peaks indicate relative enrichment of ions at that distance in the 8-nanoparticle system, while negative values denote relative depletion. The figure clearly shows a pronounced positive peak at $r \approx 2.5$ Å, confirming that nanoparticle addition leads to enhanced ion accumulation in this region; a negative peak appears at a slightly larger distance of $r \approx 4.5$ Å, reflecting the migration of ions from the bulk region toward the interface. This differential curve intuitively quantifies the impact of nanoparticles on ion distribution, consistent with the potential energy reduction mechanism discussed in the main text.

Fig. 10(c) is the RDF curve of 0–8 particles of Na–Cl. At a temperature of 1400 K, as the doping amount increases, the first peak of $g_{\mathrm{Na-Cl}}(r)$ gradually shifts to the left and the peak height increases, indicating that with the increase in the number of SiO_2 nanoparticles added, the distance between the

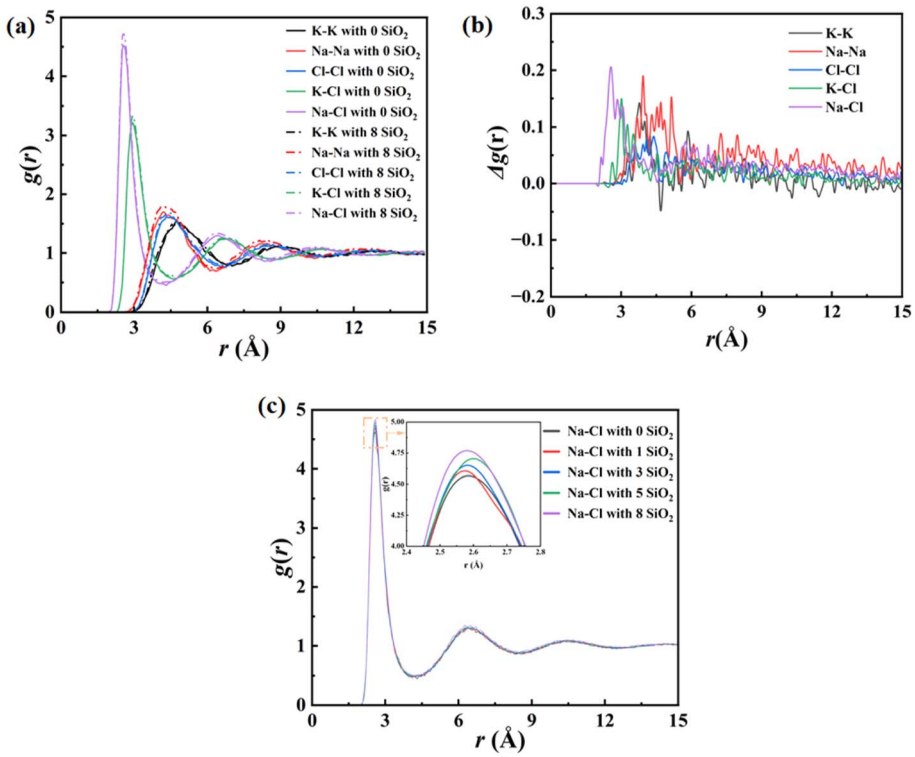

Fig. 10 (a) The $g(r)$ of ions outside the SiO_2 when $n = 0$ and $n = 8$; (b) the $g(r)$ difference map between 8 nanoparticles and 0 nanoparticles (c) the $g(r)$ of Na–Cl for different numbers of SiO_2.

anions and cations in the center ion Na^+ coordination layer decreases, the number of ligands Cl^- in the coordination layer of the center ion Na^+ gradually increases, and the interaction between the anions and cations strengthens, making the structure more dense.

3.5. Thermal diffusion properties

In order to quantitatively analyze the influence of atomic diffusion on the heat transfer characteristics, under the *NVT* ensemble, the evolution of the mean square displacement (MSD) of the molten salt system with different amounts of nanoparticles at different temperatures was recorded over time. At the same time, the corresponding self-diffusion coefficient (D) was calculated based on MSD to characterize the movement ability of atoms at different temperatures. The calculation basis of MSD and D is the Einstein relationship,[54] and the formulas are as follows: eqn (11) and (12):

$$\mathrm{MSD} = \langle |r(t) - r(0)|^2 \rangle \quad (12)$$

$$D = \lim_{t\to\infty} \frac{1}{6t} \left\langle |r(t) - r(0)|^2 \right\rangle \quad (13)$$

Here, $r(t)$ and $r(0)$ represent the position vectors of the particle at time t and 0 respectively. The MSD and D of the molten salt at different temperatures are shown in Fig. 11.

Fig. 11(a)–(e) shows the MSD at different temperatures within 200 ps. The MSD increases linearly with time and becomes larger with increasing temperature, indicating that the nanofluid is in a molten state and the diffusion ability of the atoms increases with temperature. Temperature and nanoparticle concentration significantly affect atomic mobility, which is also reflected in the self-diffusion coefficients.

The calculated D are shown in Fig. 11(f), and D increases with temperature. Table 5 lists the D values at 1000 K and 1800 K. The results show that increasing the number of SiO_2 nanoparticles decreases the D, and this trend is more pronounced at high temperatures. When the temperature increases from 1000 K to 1800 K, the D for 0, 1, 3, 5, and 8 nanoparticles increase by 357.5%, 354.2%, 364.0%, 376.8%, and 370.8%, respectively. However, the D of the molten salt nanofluid decreases with increasing SiO_2 nanoparticle concentration. At 1800 K, as the number of nanoparticles increases from 1 to 8, the D of the molten salt decreases by 2.88%, 6.83%, 10.82%, and 17.35%, respectively. This indicates that the addition of nanoparticles suppresses the average distance traveled by atoms in the simulated system, and this suppression effect increases significantly with the number of doped nanoparticles. This conclusion is corroborated by the RDF calculation results in Section 3.5, indicating that the compressed interfacial layer enhances the optimization effect of nanoparticles on the system's heat transfer characteristics. Furthermore, the existence of micro-convection effects is inferred based on kinetic evidence from the nonlinear variation of self-diffusion coefficients.

3.6. Energy analysis

Since the thermodynamic state of atoms in the system is always influenced by energy changes, studying the variations of various

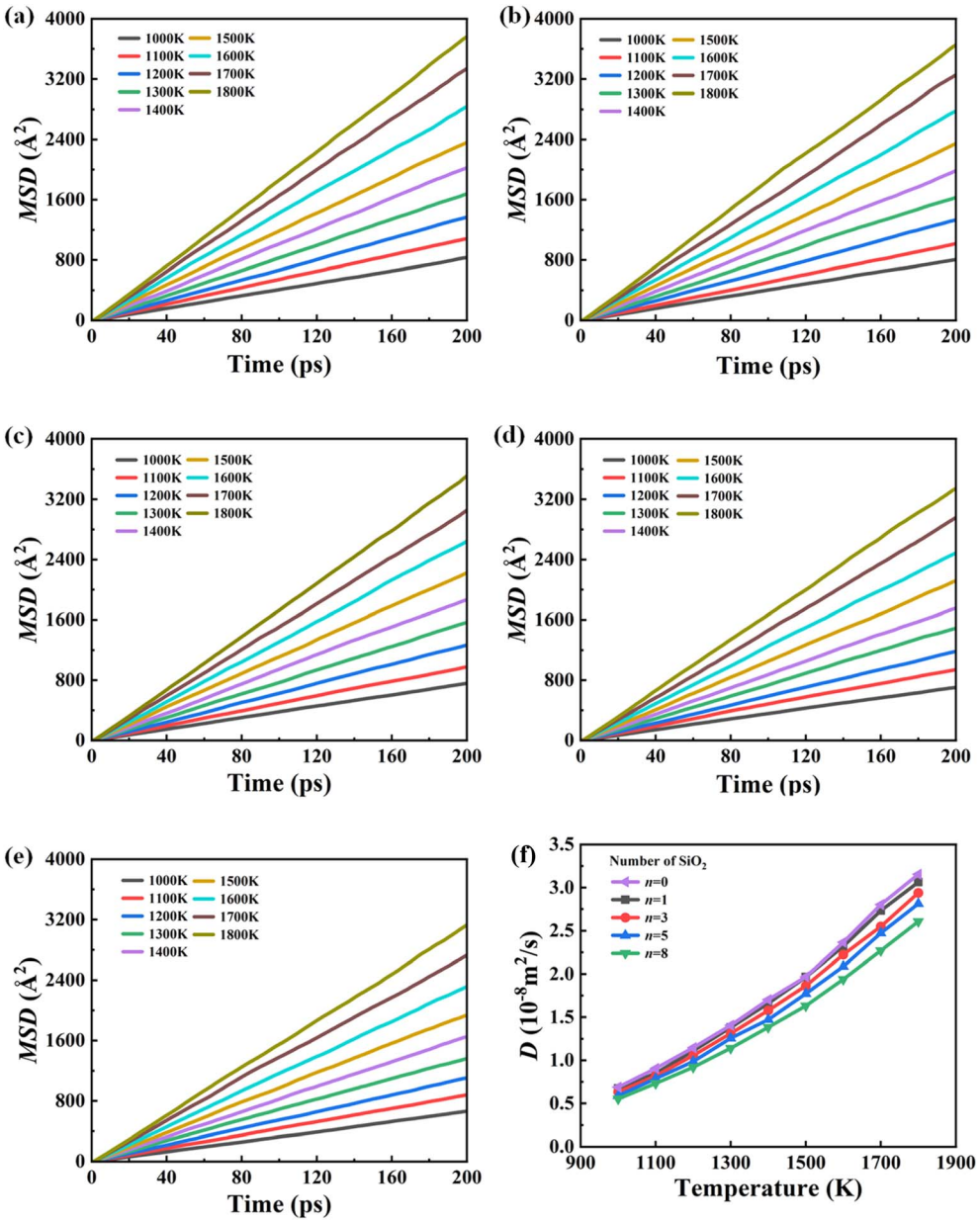

Fig. 11 Ionic diffusion abilities: (a–e) MSD of ions when $n = 0$–8; (f) D of ions when $n = 0$–8.

atomic energies is helpful for understanding the formation mechanism of the compressed interface layer. Therefore, the calculation and analysis of the average atomic energy of ions after adding different amounts of nanoparticles were carried out. In the MD simulation, the energy of each atom is composed of kinetic energy E_k and potential energy E_p, and the specific expression of the energy is as shown in formula (14):

$$E_{total} = E_p + E_k \quad (14)$$

The average atomic kinetic energy and potential energy of the ions after adding different amounts of nanoparticles were calculated and analyzed. Fig. 12 shows the E_p and E_k of K^+, Na^+, and Cl^- ions in the composite molten salt at 1400 K.

The results show that the kinetic energy fluctuations of the three types of ions are relatively small. According to the fluctuation–dissipation theorem in statistical mechanics and the calculation of statistical errors, the average atomic kinetic energy is roughly the same, indicating that the calculation results are consistent with the equipartition theorem.[55] The potential energy of the ions changes with the number of SiO_2 nanoparticles. As the number of nanoparticles increases from 0 to 8, the average potential energy of K^+ and Na^+ ions decreases by 2.33% and 1.65%, respectively, while the average potential energy of Cl^- ions increases by 1.45%. This is due to the attraction and repulsion of cations and anions by SiO_2 nanoparticles, respectively. Therefore, increasing the number of nanoparticles can effectively enhance the association between

Table 5 Self-diffusion coefficients of CTES materials at 1200 K and 1800 K

Temperature (K)	Number of SiO_2	D (10^{-8} m^2 s^{-1})
1000	0	0.6895
	1	0.6745
	3	0.6334
	5	0.5899
	8	0.5537
1800	0	3.1542
	1	3.0635
	3	2.9388
	5	2.8129
	8	2.6069

cations and anions, and the formation of the compressed interfacial layer is due to the accumulation of Na^+ and K^+ on the surface of the nanoparticles. The accumulation of cations at nanoparticle surfaces is well documented in the literature. Both experimental and theoretical studies consistently demonstrate that monovalent cations (including Na^+ and K^+) enrich at the interface of negatively charged nanoparticles. For instance, Kewalramani *et al.*[56] directly probed the radial distribution of cations around spherical nucleic acid–gold nanoparticle conjugates using small-angle X-ray scattering (SAXS) combined with classical density functional theory (DFT). They reported that the average cation concentration in the SNA shell could be enhanced by up to 15-fold, depending on the bulk solution ionic concentration. This study provides direct experimental validation that Na^+ and K^+ indeed accumulate at nanoparticle surfaces in a distance-dependent manner. Although species-resolved density distributions would constitute ideal evidence, the overall consistency with the literature supports our conclusions.

The observed decrease in system potential energy with increasing nanoparticle number is consistent with the conclusion that cation-enriched layers form at SiO_2 interfaces, a phenomenon extensively documented in the literature. Svobodova-Sedlackova *et al.*[57] discovered through molecular dynamics simulations that semi-ordered ionic layers rich in Na^+ cations form around nanoparticles in SiO_2-doped $NaNO_3$ molten salts, with this microstructure directly resulting in a 26% enhancement in specific heat capacity at 1 wt% doping concentration. Similarly, simulation studies by Wen *et al.*[58] on SiO_2-embedded nitrate ($NaNO_3$–KNO_3) and carbonate molten salts revealed that the surface charge of nanoparticles induces ordered stratified distribution of molten salt ions near the interface, leading to elevated local electrostatic potential energy at the nanoparticle surface. Consequently, ionic layers of the same charge type become more prone to expansion upon heating, generating larger local thermal expansion coefficients—the microscopic origin of thermal property enhancement.

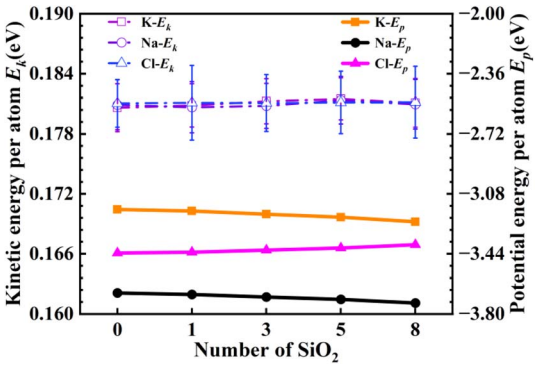

Fig. 12 Average kinetic energy and potential energy of molten salt ions in the systems.

The surface charge mechanism attracting cations has been quantified experimentally: Jeong and Jo[59] measured the zeta potential of SiO_2 nanoparticles in nitrate solutions, finding that zeta potential increases linearly with $NaNO_3$ composition, and demonstrated through electrical double layer analysis that the electrical double layer interaction potential in the vicinity of nanoparticles governs the specific heat capacity enhancement of molten salt nanofluids. Gmür *et al.*[60] conducted quantitative investigations of surface potential and charge density at silica nanoparticle–electrolyte interfaces using potentiometric titration, ATR-FTIR, and XPS, conclusively confirming that under negatively charged SiO_2 conditions, the identity of cations (Li^+, Na^+, K^+, Cs^+) significantly influences surface charge density and surface potential. This effect can be explained by the closest approach distance determined by cation hydration diameters. The consistency between our observations and these established research findings supports the interpretation that "compressed ionic interfacial layers drive thermal property enhancement".

4 Discussion

(1) This work employs a classical force field based on the pair-potential approximation, where cross-interaction parameters are obtained from mixing rules without rigorous DFT validation. Future research could utilize *ab initio* molecular dynamics (AIMD) or machine learning potentials for precise fitting of ion–surface interactions to further validate the quantitative accuracy of the present findings.

(2) Although the present work provides qualitative evidence for ion accumulation at the nanoparticle interface, future studies should focus on quantitative characterization, including (i) calculation of excess ion numbers within the first coordination shell (≈6 Å) *via* molecular dynamics simulations following the approach of Svobodova-Sedlackova *et al.*,[57] and (ii) experimental measurement of zeta potential for SiO_2 nanoparticles in molten salt environments as demonstrated by Jeong and Jo[59] to directly correlate surface charge with thermal property enhancement.

(3) It should be noted that there exists an optimal concentration range for nanoparticle addition, beyond which performance improvements may saturate or even deteriorate. In this study, although performance continued to increase at $n = 8$, the factors determining this optimal concentration are multifaceted: First, matrix properties significantly influence the optimal loading. Chen *et al.*[61] found that viscosity changes in polymer/

nanoparticle composites exhibit a melt chain length dependence, with longer chains showing more pronounced nanoparticle effects. This indicates that the molecular characteristics of the matrix are one of the key parameters determining the optimal doping concentration. Second, interfacial interactions are crucial. Geng *et al.*[62] demonstrated that carbon nanoparticle incorporation disrupts interfacial molecular packing density, reducing mechanical properties. In this study, the saturation of the ionic interfacial layer may be an intrinsic factor limiting continuous performance enhancement. When interfacial ion concentration becomes too high, similar reductions in packing density or disruption of ordering may occur, leading to diminished performance gains. Therefore, determining the optimal doping concentration requires comprehensive consideration of matrix properties, interfacial physics, and multi-parameter coupling. This work reveals the microscopic mechanism of ionic interfacial aggregation, providing a theoretical foundation for subsequent systematic optimization of doping conditions through response surface methodology.

(4) A phenomenon worthy of in-depth discussion is that with increasing number of nanoparticles, the average potential energy of K^+ and Na^+ decreases, while that of Cl^- increases. This may seem counterintuitive given the overall compaction of the system (increased coordination number), but it is actually an inevitable consequence of charge redistribution and the competition between different ion–ion interactions induced by the negatively charged interface. The surface of SiO_2 nanoparticles carries a negative charge, which strongly attracts cations. Cations accumulate in the interfacial region, and their enhanced attraction to the surface and to surrounding anions leads to a decrease in their potential energy. In contrast, anions are repelled by the surface and are forced to distribute outside the cation layer or within interstices between cations. As the number of nanoparticles increases, the overall ion density rises, reducing the average distance between anions and thereby enhancing anion–anion Coulomb repulsion. The theoretical framework of Harris *et al.*[63] clearly identifies three types of velocity cross-correlations in molten salts: cation–anion, cation–cation, and anion–anion; the cross-correlations between like-charged ions contribute significantly to the system's properties. Simultaneously, the accumulation of cations at the interface forms a positive charge layer that screens anions from the surface, so that anions primarily experience the mean field of the cation layer rather than direct strong attraction. Walz and van der Spoel[64] showed that variations in the strength of cation–anion bonds in molten salts affect the effective potential field experienced by ions. Moreover, the responses of anions and cations to changes in interfacial structure are decoupled. Sarou-Kanian *et al.*[65] studied molten fluorides and found that the self-diffusion coefficients of anions and cations exhibit different trends with composition, indicating that their sensitivity to structural changes differs. Therefore, opposite trends in the potential energies of cations and anions are fully consistent with the fundamental principles of molten salt physical chemistry. In summary, the increase in anion potential energy arises mainly from enhanced anion–anion repulsion and changes in the effective potential field, which does not contradict the decrease in cation potential energy due to surface attraction. Together, these effects paint a complete picture of the rearrangement of the interfacial ionic layer.

(5) Within the temperature range of 1000–1800 K, the surface chemical state of silica nanoparticles remains stable without significant surface chemical reactions. The interfacial layer thickness shows no obvious variation, while ion density decreases with increasing temperature. The physical enhancement of ionic thermal motion is the dominant mechanism responsible for the decline in ion density.

(6) This study employed the original BKS charge parameters, which were fitted based on first-principles calculations and represent the field standard for silica simulations. Systematic charge sensitivity analysis has not been conducted in this work, which constitutes one of the limitations of this study. As discussed, the core qualitative conclusions (the opposite trends in anion/cation potential energy changes, and the existence of micro-convection) originate from the physical nature of the net negative surface charge; therefore, they are expected to remain robust against reasonable variations in charge parameters. Future research will further quantify the influence of charge parameters on interfacial properties through sensitivity analysis or polarizable force fields.

5 Conclusions

Taking NaCl–KCl composite molten salt as the research object and using amorphous SiO_2 as the doping nanomaterial, multiple nanograins were randomly doped into the molten salt. A microscopic physical model for the CTES material was established. Molecular dynamics studies were carried out on its thermal properties. The thermal performance parameters, microstructural parameters, and energy parameters of the CTES material were calculated, and the microscopic mechanism of the enhanced thermal performance was revealed. The main conclusions obtained are as follows:

(1) As the number of SiO_2 nanoparticles increases from 0 to 8, the thermal conductivity, viscosity, and specific heat capacity of the molten salt nanofluid all exhibit significant enhancement. The maximum improvements are 7.08% for thermal conductivity, 51.21% for viscosity, and 8.25% for specific heat capacity. The observed increase in viscosity is a direct macroscopic manifestation of the formation of compressed ionic layers at the nanoparticle surface. This phenomenon corroborates the strengthening of interfacial microstructure, although in practical engineering applications, increased viscosity typically implies additional pumping power consumption. The tension between such microscopic mechanistic evidence and engineering performance metrics represents the core trade-off that must be carefully balanced in nanofluid research. Furthermore, the enhancement in specific heat capacity achieved by adding 8 SiO_2 nanoparticles is approximately 19 times that obtained by adding a single nanoparticle, which further confirms the pronounced influence of nanoparticle number on thermal performance.

(2) Microconvection effects were observed in the nanofluid. As the temperature increased, the diffusion ability of ions in the

molten salt was significantly enhanced. When the temperature was raised from 1000 K to 1800 K, the MSD of the base molten salt nanofluid increased by 357.5%, indicating that the ion diffusion behavior was intensified with increasing temperature. On the other hand, increasing the number of SiO_2 nanoparticles enhanced the association between cations and anions in the molten salt, making the structure more compact. At 1800 K, adding 8 nanoparticles reduced the D of the molten salt by 17.35%, indicating that the addition of nanoparticles to some extent restricted the ion diffusion behavior.

(3) The enhanced thermal performance of the NaCl–KCl molten salt nanofluid was attributed to the accumulation of Na^+ and K^+ on the surface of SiO_2 nanoparticles, forming a compressed interfacial layer with a thickness of approximately 6 Å. The presence of the interfacial layer altered the microstructure of the molten salt nanofluid, thereby improving its thermophysical properties.

Conflicts of interest

There are no conflicts to declare.

Data availability

The data supporting this study's findings are available in the main text.

Acknowledgements

This work was supported by the National Natural Science Foundation of China (No. 52576051), the University Outstanding Youth Fund Project of Anhui Province under grant (No. 2022AH020028), the Natural Science Foundation of Anhui Province under grant (No. 2308085ME173), the China Postdoctoral Science Foundation (No. 2025T180160), and the Postdoctoral Innovation Program of Shandong Province (No. SDCX-ZG-202502013).

References

1 M. T. Islam, N. Huda, A. Abdullah, *et al.*, A comprehensive review of state-of-the-art concentrating solar power (CSP) technologies: Current status and research trends, *Renewable Sustainable Energy Rev.*, 2018, **91**, 987–1018.
2 E. K. Solak and E. Irmak, Advances in organic photovoltaic cells: a comprehensive review of materials, technologies, and performance, *RSC Adv.*, 2023, **13**, 12244–12269.
3 M. Sun, T. Liu, X. Wang, *et al.*, Roles of thermal energy storage technology for carbon neutrality, *Carbon Neutrality*, 2023, **2**, 12.
4 T. Liu, Y. Rong and Y. Xiong, Spacer improvement for efficient and fully printable mesoscopic perovskite solar cells, *RSC Adv.*, 2017, **7**, 10118–10123.
5 I. Renewables, *Analysis and Forecast to 2030*, International Energy Agency, Paris, France, 2024.
6 N. Chomcharoen, T. Muangnapoh, B. Traipattanakul, *et al.*, Improvement of optical properties of AISI 304 as a solar absorber using a pulsed fiber laser, *RSC Adv.*, 2023, **13**, 22281–22286.
7 H. Tafrishi, S. Sadeghzadeh and R. Ahmadi, Molecular dynamics simulations of phase change materials for thermal energy storage: a review, *RSC Adv.*, 2022, **12**, 14776–14807.
8 A. Palacios, C. Barreneche, M. Navarro, *et al.*, Thermal energy storage technologies for concentrated solar power–A review from a materials perspective, *Renewable Energy*, 2020, **156**, 1244–1265.
9 D. R. Parida and S. Basu, On the specific heat capacity of HITEC-salt nanocomposites for concentrated solar power applications, *RSC Adv.*, 2023, **13**, 5496–5508.
10 M. Z. Mistarihi, G. M. Magableh and S. M. Abu Dalu, A hybrid solar–thermoelectric system incorporating molten salt for sustainable energy storage solutions, *Technologies*, 2025, **13**, 104.
11 M. A. Orozco, K. Acurio, F. Vásquez-Aza, A. Chico-Proano, *et al.*, Thermal storage of nitrate salts as phase change materials (PCMs), *Materials*, 2021, **14**, 7223.
12 J. H. Chen, A literature review on novel nitrate molten salt for heat storage, *Key Eng. Mater.*, 2021, **881**, 87–94.
13 B. D'Aguanno, M. Karthik, A. Grace, *et al.*, Thermostatic properties of nitrate molten salts and their solar and eutectic mixtures, *Sci. Rep.*, 2018, **8**, 1–15.
14 H. Na, C. Zhang, Y. Wu, *et al.*, Investigation on thermal performance of eutectic binary nitrate-carbonate molten salt under thermal shock condition, *Sol. Energy Mater. Sol. Cells*, 2023, **255**, 112314.
15 A. Caraballo, S. Galán-Casado, Á. Caballero, *et al.*, Molten salts for sensible thermal energy storage: a review and an energy performance analysis, *Energies*, 2021, **14**, 1197.
16 I. Arias, J. Cardemil, E. Zarza, *et al.*, Latest developments, assessments and research trends for next generation of concentrated solar power plants using liquid heat transfer fluids, *Renewable Sustainable Energy Rev.*, 2022, **168**, 112844.
17 P. Xie, X. Wei, W. Wang, *et al.*, Two new chloride eutectic mixtures and their thermo-physical properties for high temperature thermal energy storage, *International Conference on Applied Energy*, 2019.
18 H. Yin, Z. Wang, X. Lai, *et al.*, Optimum design and key thermal property of NaCl–KCl–$CaCl_2$ eutectic salt for ultra-high-temperature thermal energy storage, *Sol. Energy Mater. Sol. Cells*, 2022, **236**, 111541.
19 C. Villada, W. Ding, A. Bonk, *et al.*, Engineering molten $MgCl_2$-KCl-NaCl salt for high-temperature thermal energy storage: Review on salt properties and corrosion control strategies, *Sol. Energy Mater. Sol. Cells*, 2021, **232**, 111344.
20 W. Ding, H. Shi, A. Jianu, *et al.*, Molten chloride salts for next generation concentrated solar power plants: Mitigation strategies against corrosion of structural materials, *Sol. Energy Mater. Sol. Cells*, 2019, **193**, 298–313.
21 W. Ding, A. Bonk and T. Bauer, Corrosion behavior of metallic alloys in molten chloride salts for thermal energy storage in concentrated solar power plants: A review, *Front. Chem. Sci. Eng.*, 2018, **12**, 564–576.

22 L. Zhao, J. Wang, L. Cui, *et al.*, Performance design of high-temperature chloride salts as thermal energy storage material, *J. Therm. Sci.*, 2024, **33**, 479–490.
23 C. Li, Q. Li, X. Lu, *et al.*, Inorganic salt based shape-stabilized composite phase change materials for medium and high temperature thermal energy storage: Ingredients selection, fabrication, microstructural characteristics and development, and applications, *J. Energy Storage*, 2022, **55**, 105252.
24 A. Yadav, A. Verma, A. Kumar, *et al.*, Recent advances on enhanced thermal conduction in phase change materials using carbon nanomaterials, *J. Energy Storage*, 2021, **43**, 103173.
25 E. Hamdy, L. Saad, F. Abulfotuh, *et al.*, Enhancement of molten nitrate thermal properties by reduced graphene oxide and graphene quantum dots, *ACS Omega*, 2020, **5**, 21345–21354.
26 I. Sarbu and C. Sebarchievici, A comprehensive review of thermal energy storage, *Sustainability*, 2018, **10**, 191.
27 Y. Tao, C. Lin and Y. He, Preparation and thermal properties characterization of carbonate salt/carbon nanomaterial composite phase change material, *Energy Convers. Manage.*, 2015, **97**, 103–110.
28 Y. Cui, C. Liu, S. Hu, *et al.*, The experimental exploration of carbon nanofiber and carbon nanotube additives on thermal behavior of phase change materials, *Sol. Energy Mater. Sol. Cells*, 2011, **95**, 1208–1212.
29 G. Qiao, H. Cao, F. Jiang, *et al.*, Experimental study of thermo-physical characteristics of molten nitrate salts based nanofluids for thermal energy storage, *ES Energy Environ.*, 2019, **4**, 48–58.
30 J. Navas, A. Sánchez-Coronilla, E. I. Martín, *et al.*, On the enhancement of heat transfer fluid for concentrating solar power using Cu and Ni nanofluids: An experimental and molecular dynamics study, *Nano Energy*, 2016, **27**, 213–224.
31 H. A. Aljaerani, M. Samykano, A. Pandey, *et al.*, Thermophysical properties enhancement and characterization of CuO nanoparticles enhanced HITEC molten salt for concentrated solar power applications, *Int. Commun. Heat Mass Tran.*, 2022, **132**, 105898.
32 D. Han, B. G. Lougou, Y. Xu, *et al.*, Thermal properties characterization of chloride salts/nanoparticles composite phase change material for high-temperature thermal energy storage, *Appl. Energy*, 2020, **264**, 114674.
33 S. M. M. Rizvi and D. Shin, Mechanism of heat capacity enhancement in molten salt nanofluids, *Int. J. Heat Mass Transfer*, 2020, **161**, 120260.
34 F. Song, K. Tan, G. Wang, *et al.*, Microscopic analysis on the thermophysical properties enhancement of binary molten carbonates, *Case Stud. Therm. Eng.*, 2025, 107164.
35 G. Qiao, M. Lasfargues, A. Alexiadis, *et al.*, Simulation and experimental study of the specific heat capacity of molten salt based nanofluids, *Appl. Therm. Eng.*, 2017, **111**, 1517–1522.
36 J. Seo, A. Mostafavi and D. Shin, Molecular dynamics study of enhanced specific heat bymolten salt eutectic (Li_2CO_3-K_2CO_3) doped with SiO_2 nanoparticles, *Int. J. Multiscale Comput. Eng.*, 2018, **16**, 427–439.
37 W. Zhou, Z. Yang, Y. Feng, *et al.*, Insights into the thermophysical properties and heat conduction enhancement of NaCl-Al_2O_3 composite phase change material by molecular dynamics simulation, *Int. J. Heat Mass Transfer*, 2022, **198**, 123422.
38 X. Yang, C. Ji, J. Liu, *et al.*, New insights into the heat capacity enhancement of nano-SiO_2 doped alkali metal chloride molten salt for thermal energy storage: A molecular dynamics study, *J. Energy Storage*, 2023, **63**, 107015.
39 J. Liu and X. Xiao, Molecular dynamics investigation of thermo-physical properties of molten salt with nanoparticles for solar energy application, *Energy*, 2023, **282**, 128732.
40 S. S. Mahajan, G. Subbarayan and B. G. Sammakia, Estimating thermal conductivity of amorphous silica nanoparticles and nanowires using molecular dynamics simulations, *Phys. Rev. E: Stat., Nonlinear, Soft Matter Phys.*, 2007, **76**, 056701.
41 N. K. Kaliannan, K. Krishnamurthy, S. Sreerama, *et al.*, Monte Carlo Simulations of bulk and nano amorphous silica (a-SiO_2) melts, *Comput. Mater. Sci.*, 2018, **146**, 90–101.
42 F. Fumi and M. Tosi, Ionic sizes and born repulsive parameters in the NaCl-type alkali halides- II: The Huggins-Mayer and Pauling forms, *J. Phys. Chem. Solids*, 1964, **25**, 31–43.
43 J. Ding, G. Pan, L. Du, *et al.*, Theoretical prediction of the local structures and transport properties of binary alkali chloride salts for concentrating solar power, *Nano Energy*, 2017, **39**, 380–389.
44 N. Afify, G. Mountjoy and R. Haworth, Selecting reliable interatomic potentials for classical molecular dynamics simulations of glasses: The case of amorphous SiO_2, *Comput. Mater. Sci.*, 2017, **128**, 75–80.
45 Z. Rao, K. Ye, H. Wang, *et al.*, Effects of interface layer on the thermophysical properties of solar salt-SiO_2 nanofluids: A molecular dynamics simulation, *Int. J. Energy Res.*, 2021, **45**, 13323–13337.
46 S. Ge, X.-X. Zhang and M. Chen, Viscosity of NaCl aqueous solution under supercritical conditions: a molecular dynamics simulation, *J. Chem. Eng. Data*, 2011, **56**, 1299–1304.
47 F. Müller-Plathe, A simple nonequilibrium molecular dynamics method for calculating the thermal conductivity, *J. Chem. Phys.*, 1997, **106**, 6082–6085.
48 Y. Nagasaka, N. Nakazawa and A. Nagashima, Experimental determination of the thermal diffusivity of molten alkali halides by the forced Rayleigh scattering method. I. Molten LiCl, NaCl, KCl, RbCl, and CsCl, *Int. J. Thermophys.*, 1992, **13**, 555–574.
49 B. E. Poling, J. M. Prausnitz, O. C. John Paul, *et al.*, *The Properties of Gases and Liquids*, Mcgraw-hill, New York, 2001.
50 F. Müller-Plathe, Reversing the perturbation in nonequilibrium molecular dynamics: An easy way to calculate the shear viscosity of fluids, *Phys. Rev. E: Stat.*

Phys., Plasmas, Fluids, Relat. Interdiscip. Top., 1999, **59**, 4894–4898.

51 R. Dawson, E. B. Brackett and T. E. Brackett, A high temperature calorimeter; the enthalpies of α-aluminum oxide and sodium chloride, *J. Phys. Chem.*, 1963, **67**, 1669–1671.

52 M. W. Chase, NIST-JANAF thermochemical tables, *J. Phys. Chem. Ref. Data*, 1998, **28**, 1951.

53 B. Bhargava and S. Balasubramanian, Layering at an ionic liquid–vapor interface: A molecular dynamics simulation study of [bmim][pf_6], *J. Am. Chem. Soc.*, 2006, **128**, 10073–10078.

54 Y. Iwai, H. Higashi, H. Uchida, *et al.*, Molecular dynamics simulation of diffusion coefficients of naphthalene and 2-naphthol in supercritical carbon dioxide, *Fluid Phase Equilib.*, 1997, **127**, 251–261.

55 W. Krauth, *Statistical Mechanics: Algorithms and Computations*, OUP Oxford, 2006.

56 S. Kewalramani, J. W. Zwanikken, R. J. Macfarlane, *et al.*, Counterion distribution surrounding spherical nucleic acid–Au nanoparticle conjugates probed by small-angle X-ray scattering, *ACS Nano*, 2013, **7**, 11301–11309.

57 A. Svobodova-Sedlackova, C. Barreneche, G. Alonso, *et al.*, Effect of nanoparticles in molten salts MD simulations and experimental study, *Renewable Energy*, 2020, **152**, 208–216.

58 R. Wen, Z. Sun, Z. Huang, *et al.*, Nanoparticle surface charge-enhanced heat capacity in molten salt phase change materials, *Sol. Energy Mater. Sol. Cells*, 2022, **239**, 111795.

59 S. Jeong and B. Jo, Distinct behaviors of KNO_3 and $NaNO_3$ in specific heat enhancement of molten salt nanofluid, *J. Energy Storage*, 2023, **68**, 107789.

60 A. Gmür, A. Goel and M. A. Brown, Quantifying specific ion effects on the surface potential and charge density at silica nanoparticle–aqueous electrolyte interfaces, *J. Phys. Chem. C*, 2016, **120**, 16617–16625.

61 T. Chen, H. Y. Zhao, R. Shi, *et al.*, An unexpected N-dependence in the viscosity reduction in all-polymer nanocomposite, *Nat. Commun.*, 2019, **10**, 5552.

62 Y. Geng, Q. Zhao, J. Wang, *et al.*, Evaluating the impact of carbon nanoparticles on the interfacial properties of the pulmonary surfactant film, *Nanomaterials*, 2025, **15**, 1244.

63 K. R. Harris and M. Kanakubo, Effect of relative mass on ion velocity cross-correlations in ionic liquids and molten salts: different perspectives in different reference frames, *J. Phys. Chem. B*, 2024, **128**, 4504–4512.

64 M. M. Walz and D. van der Spoel, Molten alkali halides – temperature dependence of structure, dynamics and thermodynamics, *Phys. Chem. Chem. Phys.*, 2019, **21**, 18516–18524.

65 V. Sarou-Kanian, A. L. Rollet, M. Salanne, *et al.*, Diffusion coefficients and local structure in basic molten fluorides: in situ NMR measurements and molecular dynamics simulations, *Phys. Chem. Chem. Phys.*, 2009, **11**, 11501–11506.